


RESEARCH ARTICLE

Power-effective scanning with AODs for 3D optogenetic applications

Pietro Ricci^{1,2*}  | Marco Marchetti³ | Michele Sorelli^{1,2} | Lapo Turrini^{1,2} |
Francesco Resta^{1,2} | Vladislav Gavryusev^{1,2} | Giuseppe de Vito^{1,4} |
Giuseppe Sancataldo⁵ | Francesco Vanzi^{1,6} | Ludovico Silvestri^{1,2,7} |
Francesco Saverio Pavone^{1,2,3,7}

¹European Laboratory for Non-Linear Spectroscopy, Florence

²Department of Physics and Astronomy, University of Florence, Florence

³L4T-Light4Tech, Florence, Italy

⁴Department of Neuroscience, Psychology, Drug Research and Child Health, University of Florence, Florence, Italy

⁵Department of Physics and Chemistry, University of Palermo, Palermo, Italy

⁶Department of Biology, University of Florence, Florence, Italy

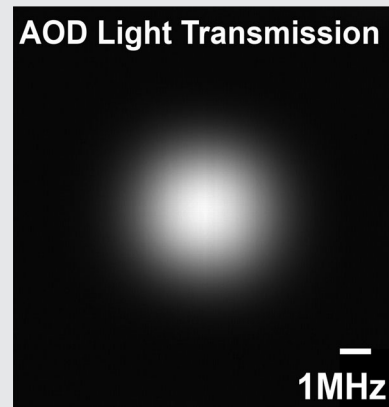
⁷National Institute of Optics, Florence, Italy

*Correspondence

Pietro Ricci, European Laboratory for Non-Linear Spectroscopy, Sesto Fiorentino, Florence 50019, Italy.
Email: ricci@lens.unifi.it

Abstract

Two-photon (2P) excitation is a cornerstone approach widely employed in neuroscience microscopy for deep optical access and sub-micrometric-resolution light targeting into the brain. However, besides structural and functional imaging, 2P optogenetic stimulations are less routinary, especially in 3D. This is because of the adopted scanning systems, often feebly effective, slow and mechanically constricted. Faster illumination can be achieved through acousto-optic deflectors (AODs) although their applicability to large volumes excitation has been limited by large efficiency drop along the optical axis. Here, we present a new



This project has received funding from the ATTRACT project funded by the EC under Grant Agreement 777222 and from the H2020 EXCELLENT SCIENCE—European Research Council (ERC) under grant agreement ID n. 692943 BrainBIT. This project has also received funding from the European Union's Horizon 2020 Framework Programme for Research and Innovation under the Grant Agreement No. 871124 (Laserlab-Europe) and was supported by the EBRAINS research infrastructure, funded from the European Union's Horizon 2020 Framework Programme for Research and Innovation under the Specific Grant Agreement No. 945539 (Human Brain Project SGA3). This research has also been supported by the Italian Ministry for Education, University, and Research in the framework of the Advance Lightsheet Microscopy Italian Mode of Euro-Bioimaging ERIC. Vladislav Gavryusev is funded by a Marie Skłodowska-Curie Fellowship (MSCA-IF-EF-ST "MesoBrainMic" grant agreement No. 793849).

This is an open access article under the terms of the Creative Commons Attribution-NonCommercial-NoDerivs License, which permits use and distribution in any medium, provided the original work is properly cited, the use is non-commercial and no modifications or adaptations are made.

© 2022 The Authors. *Journal of Biophotonics* published by Wiley-VCH GmbH.

AOD-based scheme for 2P 3D scanning that improves the power delivery between different illumination planes. We applied this approach to photostimulate an optogenetic actuator in zebrafish larvae, demonstrating the method efficiency observing increased activity responses and uniform activation probabilities from neuronal clusters addressed in the volume. This novel driving scheme can open to new AOD applications in neuroscience, allowing more effective 3D interrogation in large neuronal networks.

1 | INTRODUCTION

Understanding the computational rules of the brain, and how they are disrupted by pathologies, is one of neuroscience's main goals. To shed light on causal interactions in complex neuronal networks, we need biological methods and optical technologies enabling the recording and perturbation of neuronal clusters over large fields of view (FOVs) with high spatiotemporal resolution [1]. The first step forward toward these results has been moved owing to genetic engineering. The introduction of genetically encoded optical probes such as fluorescent calcium indicators [2, 3] and optogenetic actuators [4, 5] revolutionized the approach to the study of neuroscience. Today, those optical probes enable cell-specific targeting monitoring of neural activity by means of intracellular calcium transients and photostimulation of neurons to control their activity. Even though several advancements in optical imaging allowed the use of calcium indicators to monitor neuronal dynamics [6, 7], light-based cell perturbation methods, conversely, are still an open research field. They continuously strive for improved accessible volumes, higher speed and flexibility of targeting dynamics and optimized modularity for the simultaneous stimulation of several cells.

Nowadays, the combination of laser scanning methods with multiphoton excitation brought manifold benefits to the investigation of several kinds of biological processes [8–10]. With respect to one-photon (1P) excitation, two-photon (2P) illumination guarantees stricter spatial confinement and deeper optical access. The latter, in particular, is due to the reduced light-scattering effects in biological tissues [11] and to the lower absorption probability that characterizes the 2P fluorescence process. Indeed, with 1P excitation, many photons are absorbed before reaching the target, whereas greater depths are achieved with 2P illumination with almost full excitation power [12].

However, mechanical constraints, low efficiency in light delivery and slow dynamics have often limited the applicability of several devices in 3D 2P excitation experiments. In particular, galvanometer mirrors (GMs) are mainly utilized in 1P optogenetic studies [13, 14] and

only rarely in 3D 2P photostimulation applications [15]. Being strongly affected by mechanical inertia (tens of micrometers in $\sim 100 \mu\text{s}$ [16]), GMs provide a slow sweeping rate [17], making them not suited to rapidly access neurons spanning over extensive volumes. Several approaches have been proposed to extend the use of GMs to faster 3D applications, coupling them with remote focusing systems based on optics [18, 19], or obtained through piezo stages [20], deformable mirrors [21] and spatial light modulators (SLMs) [22].

Efforts to overcome these limitations have led to the development of several optical approaches to parallelize light targeting [23]. These enable multisite stimulation either by intensity or phase modulation, delivering light simultaneously to many targets at once and guaranteeing spatiotemporal flexibility. In specific, many early parallel photostimulation experiments adopted micro-LEDs [24], digital micromirrors devices [25–28] or liquid crystal displays [29]. However, all of these devices share the general drawback of a poor stimulation efficiency when addressing sparsely distributed targets, thus precluding their use in 2P excitation applications. Conversely, 2P optogenetics has been demonstrated with the generalized phase-contrast method [30] and using computer-generated holography [31] by means of liquid-crystal-based SLMs.

All these parallel illumination techniques suffer a low illumination efficiency since the laser power is split among all preselected targets [32]. Anyway, the power levels commonly needed for photostimulation experiments are easily reachable with high-power commercial laser sources, allowing in principle the simultaneous addressing of large numbers of cells under 2P excitation. However, the maximum power that could be delivered to the sample—and thus the maximum number of addressable spots—is limited by the heating damage threshold [33]. Indeed, by increasing the number of targets illuminated at once, the total energy released on the sample is increased as well, raising the sample photodamage probability. In addition, the limited refresh rate of SLMs prevents the possibility of tuning the radiation delivery time to reduce phototoxicity.

In this regard, commercially available SLMs guarantee a refresh rate of up to 300 to 400 Hz. This rate fits the

time bottleneck for continuous optogenetic stimulation, which is dictated by the optogenetic actuator closing rate—or channel off-gating (10–100 ms) [34]. On the other hand, the dynamics for the ion channel opening is faster: after photoexcitation, the photocurrent induced by the flowing ions rises quickly (e.g., ChR2 channel on-gating: 200 μ s), reaching the peak of maximum conductivity in 1 to 2 ms [34]. Thus, when considering multispot sequential photostimulation, the relevant scan dynamics can be tailored on the minimum required residence time of the laser for inducing the on-response in each cell. This means that the use of SLMs, although fit to the single actuator duty cycle, limits the possibility of studying the dynamics of neuronal circuits by stimulating multiple actuators in the minimum required time.

Acousto-optic deflectors (AODs) are one of the most valuable alternatives to improve the stimulation refresh rate with respect to all the aforementioned techniques [35]. AOD technology can be used to rapidly sweep the light beam and change its focusing without any mechanical movement or intrinsic inertia [36].

Interestingly, the AOD response time is constant, as it does not depend on whether subsequent points are contiguous or not. AODs are then characterized by high precision and reproducibility in beam positioning and offer high flexibility in targeting nonsequential regions of interest (ROIs), thus enabling 3D random-access scanning. In particular, AODs provide the ability to perform jumps between distant spots or to generate independent multiple beams [37–41], when rapidly changing or multiple synchronous radio frequencies (RFs) are used to drive them. In this regard, AODs are conveniently adopted for imaging applications involving multisite neuronal activity recording, which require near-microsecond temporal resolution [42–51].

Differently from parallel approaches, the AOD's capabilities to simultaneously direct light to spatially sparse targets are technically constrained to regular geometries even when using a multiple synchronous RF driving scheme. On the other hand, it is straightforward to illuminate sparse targets in a sequentially fast fashion by leveraging the AOD refresh rate (10–30 μ s). This enables to reach MHz-order dynamics and to potentially fulfill the temporal requirements for the concurrent activation of spatially distributed neurons. Indeed, by using AODs a quasi-simultaneous activation of multiple targets is potentially achievable within the same time required by a parallel approach to perform an equivalent stimulation pattern.

Despite these fundamental advantages, state-of-the-art AOD-based optogenetic applications have been so far limited to 1P neuronal photostimulation in 2D [52, 53]. Indeed, the intrinsic dependency of the AO cell diffraction efficiency

on the drive acoustic frequency has so far limited the suitability of these devices for 3D optostimulation experiments. More specifically, the power transmission of these devices drops rapidly when scanning along the optical axis. For *in vivo* imaging applications, this shortcoming leads to a reduction in signal-to-noise ratio that may limit the possibility of catching small activity events. Nonetheless, functional imaging is usually based on the analysis of the relative fluorescence expression with respect to baseline ($\Delta F/F$), which is less sensitive to global variations in the delivered power. On the other hand, in 3D optogenetics applications, the large power drop observed away from the focal plane is a fundamental limit since the actuator excitation probability is proportional to the square of the optical intensity.

Therefore, a compensation software module tuning the driving signal frequency and intensity for each addressed point is frequently used to counteract this lack of uniformity. In detail, the peak intensity released in the center of the axial scan is lowered down to the level obtained at the boundaries so that a uniform power distribution is achieved. Although such an approach can effectively flatten the power distribution across the scanned volume [49], the resulting intensity is decreased to the original minimum value.

In this work, we present an alternative solution to the power inhomogeneity of 3D AOD-based scanning systems, able to raise the axial delivery distribution toward the maximum achievable value. In order to improve the power released within the pixel dwell time, the frequency ramps driving the AODs are triggered repeatedly, effectively multiplying the minimum energy deposited on different focal planes up to five times.

With this proof-of-concept work, not only did we find an alternative to enhance the AOD axial scanning, but we enabled new applications in the volume that were hampered until now. In this regard, we demonstrated the 2P-photoactivation of optogenetic actuators expressed in zebrafish larvae. In particular, we recorded the electrophysiological activity of neuronal clusters displaced in a volume of tissue, demonstrating a more efficient axial scanning by observing larger neuronal responses compared to the original unoptimized stimulation approach, and a neuron activation probability always higher than 75%.

2 | MATERIALS AND METHODS

2.1 | AOD-based optical design

In order to achieve a laser scanning system characterized by deep optical access, large light-addressable areas and fast light-targeting dynamics, a hybrid solution composed

of four AODs and a GM head was implemented (Figure 1A).

The fundamental mechanism of AOD-based light deflection resides in a periodical change of the refractive index of its internal crystal. This is induced by a propagating sound wave generated by a vibrating piezo [54]. Thus, the transparent crystal behaves like an optical grating, which diffracts the impinging laser beams.

The designed system takes advantage of the combined use of four AODs, arranged as two identical pairs of orthogonally oriented devices, each having the first and second AOD, respectively, assigned to the x and y lateral axes. The separate AODs are driven by linearly changing RF signals $f(t) = f_{\min} + at$, where a is the slope of the frequency ramps or chirp parameter. In detail, the AODs corresponding to the same axis are driven simultaneously by counterpropagating waves. As demonstrated elsewhere [44, 54], this arrangement globally works as a variable AO lens (AOL) that generates the following beam deflection:

$$\theta(x, t) = -\left(\frac{2\lambda\alpha}{\nu^2}\right)x + \frac{\lambda}{\nu}(f_{2C} - f_{1C}) \quad (1)$$

$$F_{AOL} = \frac{\nu^2}{2\lambda\alpha} \quad (2)$$

where ν is the propagation speed of the acoustic wave in the crystal, λ is the wavelength of the laser and f_{2C} and f_{1C} are the central frequencies of the ramps driving the first and second conjugated AODs, respectively. Here, the first term is the focal length F_{AOL} of the AOL, dependent on the chirp, whereas the second term indicates the induced light beam lateral deflection.

The AOL affects the light-beam divergence and the total magnification of the optical path, determining an axial displacement that propagates up to the image plane under the objective (Figure 1B). More specifically, we have:

$$\Delta Z = \frac{F_1^2 M^2}{F_{AOL}} = k \cdot \alpha \quad (3)$$

where F_1 is the focal length of the first lens after the second AOD stage and M is the optical magnification factor regarding the subsequent optics. To summarize, with two coupled AODs, it is possible to independently control the deflection along one lateral direction and the axial positioning of the beam.

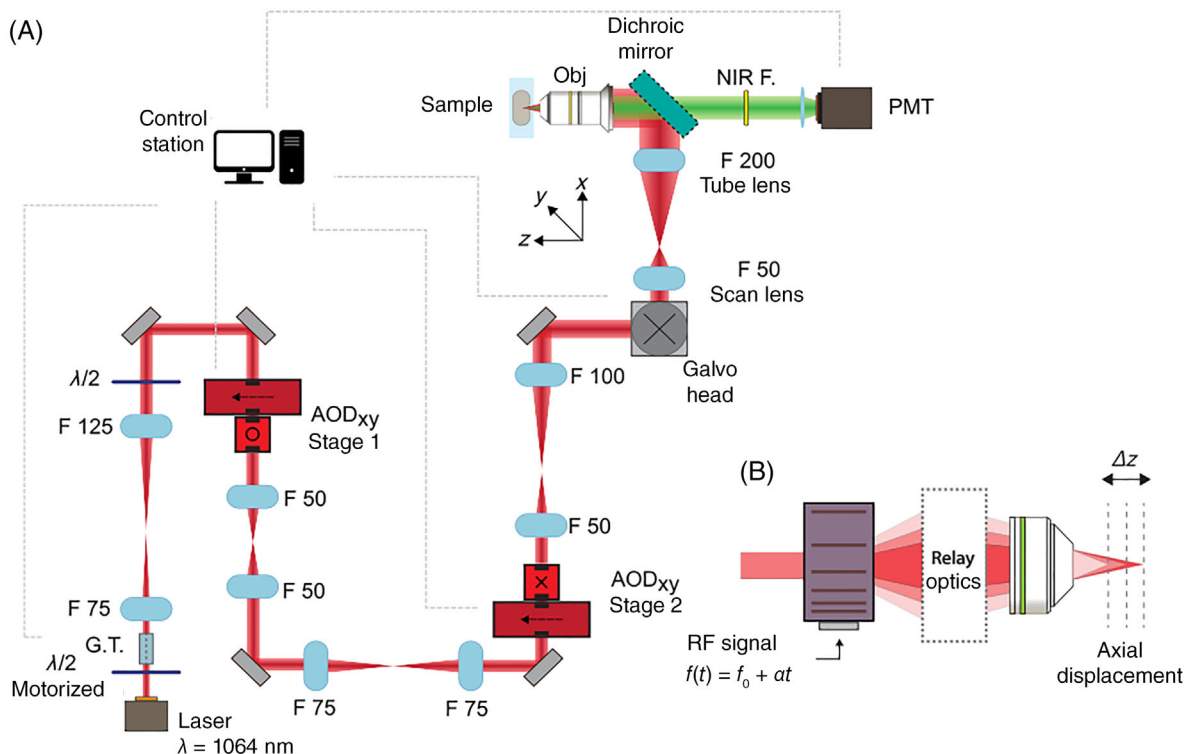


FIGURE 1 Schematic of the AOD-based scanning head. A, Optical setup with hybrid galvo-AOD scanning head implemented for 2P excitation. B, Optical diagram of the AOL focusing performance and the induced axial displacement with respect to the inherent objective focal plane. 2P, Two-photon; AOD, acousto-optic deflector; AOL, acousto-optic lens; F, focal length; G.T., Glan-Taylor polarizer; NIR F, near-infrared filter; RF, radio frequency

The proper use of four AODs enabled precise light targeting of any point in the volume and a quick modulation of the stimulation pattern. Furthermore, even though characterized by slower targeting dynamics with respect to the AO scanning, a larger optical FOV was obtained by coupling the former AOD unit with a GM scanning head. The integration of the two scanning heads, achieved with a dedicated optical design, enabled the visualization of each macro-ROI selected in the GM's FOV and the recording and fast manipulation of neurons within smaller regions defined by the AOD scanning range.

The hybrid scanning system was developed as a stand-alone add-on module to be coupled with standard microscopes. In order to validate its performance, in the present work, the system was coupled with a Leica DM LFSFA Microscope (Leica Microsystems GmbH, Wetzlar, Germany) for 2P imaging and photostimulation tests. Analogously to what was debated for lateral scanning, a slow but wide-ranging axial scanning was provided by the Leica objective stepper motor, whereas fast-axial displacement was achieved using the AODs.

The light source consists of a 1064-nm pulsed laser (FP-1060-5-fs Fianium FemtoPower, NKT Photonics, Birkerød, Denmark), characterized by a pulse duration shorter than 200 fs, a repetition rate of 80 MHz and a maximum power of 5 W. The laser beam is first directed through a half-wave wave plate (10RP02-34 Newport Corp., Irvine, California) to shift its polarization and then conveyed through a Glan-Taylor polarizer (GTH5-B Thorlabs Inc., Newton, New Jersey). The wave plate is positioned in a software-controlled rotator (MDL NSR1 Newport) allowing adjustment of the outgoing beam power, without altering its polarization.

The beam is then expanded by a factor $\times 1.66$ using a telescope (AC254-075-B-ML Thorlabs $F = 75$ mm and AC254-125-B-ML Thorlabs $F = 125$ mm), and its polarization is optimized by a second $\lambda/2$ wave plate (10RP02-34 Newport) before reaching the first pair of AODs (DTSXY-400 AA Opto Electronic, Orsay, France).

In order to optically couple the outgoing beam to the second AOD pair, light is first directed into two 1:1 relay systems comprising two 50-mm lenses (AC254-050-B-ML Thorlabs) and two 75-mm lenses (PAC19AR.16 Newport), respectively. In this way, independently of the RF applied to the first couple (and therefore regardless of the outgoing beam direction), the laser beam reaches a pivot located at the center of the second AOD stage.

The beam is then expanded $\times 2$ by a 1:2 relay (PAC17AR.16 Newport $F = 50$ mm and PAC12AR.16 Newport $F = 100$ mm) and conveyed to the center of the GMs (GVS112 Thorlabs), preceding a scan lens (AC254-050-B Thorlabs). This is optically coupled with the tube

lens of the Leica DM LFSFA, producing a further $\times 4$ magnification of the beam size. A dichroic short pass mirror (NENIR20A Thorlabs), positioned inside the Leica DM LFSFA before the objective, is used to reflect the excitation light toward the objective ($\times 20$ XLUMPLFLN Olympus Corp., Tokyo, Japan) and to transmit the fluorescence emitted by the sample onto the photomultiplier tube (PMT) detector (H7422P-40 Hamamatsu Photonics, Hamamatsu, Japan), through a NIR absorptive filter.

2.2 | Digital interface and electronic design

A graphical user interface (GUI) was developed in LabVIEW (National Instrument Corp., Austin, Texas) to operate the scanning system. The software employs two National Instrument boards (PCI-6251 and PXIe-6738) to record the fluorescence signals collected by the PMT and to interface with an Arduino Due microcontroller used to program the direct digital synthesizer (DDS, AD9959 PCBZ Analog Devices Inc., Norwood, Massachusetts) driving the AODs. By integrating the control drivers of the wave plate rotator and the GMs, the software also enables the remote adjustment of laser power transmission, FOV size and resolution. Moreover, the LabVIEW GUI allows the efficient and user-friendly design of suitable optogenetic stimulation patterns without directly exposing the configuration parameters of the AOD scanning unit. The desired scanning configuration is interpreted by a dedicated Python node, which transmits via USB the corresponding sequence of encoded data words to the Arduino board. Specifically, 3D random-access positioning of the laser beam is achieved by setting the lower and upper frequencies of the chirps generated on each RF channel and properly tuning their discrete time and frequency steps. Each data transfer from the Arduino microcontroller to the DDS channels lasts a minimum commutation time of 20 μ s, that is, the minimum beam positioning time achievable in the scanned volume (for further details, see “AOD scanning unit programming and operation rates” in the Supplementary Materials).

2.3 | Zebrafish transgenesis and maintenance

We generated a zebrafish Tg(elavl3:ReaChR-TagRFP) line using a tol2 plasmid with elavl3 promoter that drives the expression of the red-shifted light-gated cation channel ReaChR in all differentiated neurons [55, 56]. We injected the plasmid vector along with transposase mRNA into one-cell stage zebrafish embryos. Mosaic

transgenic larvae displaying strong TagRFP fluorescence at 48 hours postfertilization were selected and raised to adulthood. Offspring from one single selected founder was finally used to establish the new stable transgenic line used for the experiments.

Larvae used in the experiments—Tg(elavl3:ReaChR-TagRFP) and Tg(elavl3:H2B-GCaMP6s), *slc45a2*^{b4/b4} [57, 58] *albino* background—were maintained at 28.5°C in fish water (150 mg/L Instant Ocean, 6.9 mg/L NaH₂PO₄, 12.5 mg/L Na₂HPO₄; conductivity 300 μ S/cm, pH 7.2) under 14/10-hour light/dark cycle, according to standard procedures [59]. Larvae of the Tg(elavl3:ReaChR-TagRFP) were raised in 0.003% N-phenylthiourea (P7629 Sigma-Aldrich) to inhibit melanogenesis, avoiding the formation of skin pigments.

2.4 | Zebrafish larvae preparation

Zebrafish larvae were mounted as previously described [60]. Briefly, every 5 days postfertilization, they were transferred into a reaction tube containing 1.5% (wt/vol) low-gelling-temperature agarose (A9414, Sigma-Aldrich) in fish water, maintained fluid at 38°C. Larvae were then placed inside a glass capillary (I.D. 0.86 mm; B150-86-10, Sutter Instrument). Upon gel polymerization, they were extruded and laid on a microscope slide, with the dorsal portion facing upward. A drop of melted agarose was used to block larva orientation. Using a scalpel, we then removed part of the gel, leaving the left or the right half of the head accessible to the electrode, while keeping the animal embedded in agarose. To avoid movement artifacts during measurements, the larva was then paralyzed by 10-minute treatment with 2 mM d-tubocurarine (93750, Sigma-Aldrich), a neuromuscular blocker. After drug washout, the mounted larva was placed inside a petri dish (\varnothing 90 mm) filled with fish water kept at 28.5°C throughout the whole experiment.

2.5 | Electrophysiology recording

Local field potentials (LFPs) were recorded using a borosilicate glass microelectrode (8–10 M Ω), backfilled with a filtered solution of 2 M NaCl and 0.1 mM sulforhodamine 101 (S7635, Sigma-Aldrich) to allow the electrode tip imaging. The microelectrode was placed under visual guidance into the larval hindbrain at 150–200 μ m depth. Voltage signals were recorded using an Axopatch 200B amplifier (Molecular Devices, San Jose, California), low-pass filtered at 2 kHz and digitized at 10 kHz using a USB-621 interface (National Instruments).

2.6 | LFP data analysis

The whole data set was analyzed with Origin Pro (Version 2019, OriginLab Corporation, Northampton, Massachusetts). LFP signals were detrended using a 0.1-Hz high-pass filter and segmented in a 1-second peristimulus window. For each stimulus, we evaluated the LFP response peak amplitude. For each larva, we calculated the mean value of the peak amplitudes collected in the unchirped configuration, that is, $\alpha = 0$ MHz/ μ s, and we separately normalized the data sets with respect to this value. Mean and relative standard errors were calculated for each chirp value subset.

For the volume scanning data set, two subsets were defined, that is, single-trigger (ST) and multittrigger (MT) configurations, which were normalized with respect to ST subsets.

Regarding probability analysis, we first processed the background baseline of the traces, evaluating its mean and standard deviation for each examined trigger modality and chirp value. LFP peak amplitudes, normalized with respect to the unchirped subset as previously described, were deemed as positive events if passing a threshold equal to three times the baseline standard deviation. We finally defined the activation probability as the ratio between positive evoked events to the totality of the cases.

3 | RESULTS

3.1 | Multittriggered light stimulation

Although AODs provide very fast inertia-free deflection and focusing, they also suffer from few limitations. The first intrinsic drawback is related to their diffraction efficiency. Indeed, even though the optical transmission of each separate AOD may be as large as 95% for the first diffracted order, when assembled in the crossed XY geometry, the overall light transmission efficiency of the deflector stage is declared to be around 50%. This implies that the efficiency of the four-AOD beam-scanning unit is approximately 25%. Therefore, an adequate laser source, ensuring enough output power to compensate for these losses, is required for optostimulation applications.

Secondarily, the optical transmission is also a function of the RFs applied to the AOD. In particular, each AOD is characterized by a narrow input acceptance angle beyond which the output transmission efficiency drops considerably (for further details, see the “Optical characterization” in Supplementary Materials). In other words, light transmission through the second stage depends on the deflection induced by the first stage.

When these devices are exploited to manipulate the beam focusing, chirped signals are sent to drive the AOD, with frequencies that span a certain bandwidth. A restricted bandwidth around the center would deviate the beam by a small amount, guaranteeing the maximum transmission efficiency through the second couple. Then, clearly, the time required to address a narrower frequency band will be proportionally shorter than the one necessary for a larger bandwidth. However, even though the ramp slope—that is, the chirp value $\alpha = \Delta f/\Delta t$ —remains the same, the second case would involve frequencies that provide a less efficient light transmission far from the center. The latter case is representative of what happens when a single signal—or ST—is sent to the AOD scanning system with no bandwidth optimization (Figure S2D in the Supplementary Materials shows the light transmission of the second stage as a function of the frequency applied to the first stage).

This configuration also implies that the energy deposited on different axially displaced planes is not constant but inversely proportional to the chirp parameter. Indeed, recalling Equation (3), addressing distant planes requires large axial displacements of the AOL focus, which in turn require steeper frequency ramps with shorter duration. In such a way, a single frequency sweep leads to a progressive decrease in delivered power for increasing axial distances. On the other hand, the point-to-point dwell time ΔT cannot be freely modified but as mentioned in Section 2.2, it is constrained by the commutation time of 20 μs for the digital reconfiguration of the coordinates.

Therefore, to modulate the axial drift, we developed a novel method of signal triggering. First of all, to maximize the power transmission from the second stage, we constrained as much as possible the first-stage ramping dynamics within a very narrow high-efficiency frequency window, $\Delta f_{\text{eff}} = 1$ MHz, around the center of the AODs effective bandwidth ($f_c = 75$ MHz). Then, in order to tune the chirp, we varied the effective ramp time Δt_{chirp} , that is, the actual time required to sweep the AOD driving frequency between the limits of the high-efficiency window Δf_{eff} .

Despite the varying ramp times, the axial inhomogeneity in energy delivery could be significantly reduced through the fine configuration and repeated generation of the frequency ramps driving the AOD systems. Specifically, to raise the energy supplied to a given target volume within the dwell time, we envisaged illuminating it multiple times—or MT—instead of only once.

For each sequentially addressed coordinate, we computed how many repetitions of a single narrow frequency sweep completely fit the point dwell time. In detail, the number of applied triggers (rounded to the lower nearest

integer) is $N_{\text{trigger}} = \Delta T/\Delta t_{\text{chirp}}$. In such a way, the total energy delivered during the ΔT is a multiple of the energy conveyed in response to a single frequency ramp: $P_{\text{MT}} = P_{\text{ST}} \times N_{\text{trigger}}$.

A further consideration about the minimum frequency sweeping time is however required at this stage. Namely, the resulting Δt_{chirp} must not be allowed to drop below the lower threshold represented by the AOD access time dt . That is, the time required by the acoustic wave to cross the AOD internal crystal and interact with the beam spot, steering light toward the target position. More specifically, the access time is needed to prevent light from simultaneously interacting with consecutive frequency ramps, which would lead to a spurious splitting of the input laser beam and, consequently, to the parallel interaction with distinct spatial coordinates of the sample. In practice, if the above condition is not satisfied, “ghost images” would emerge during image acquisition. In our configuration, the effective access time is $dt = 4$ μs (for further details about the estimation of this parameter, see “Optical characterization” in Supplementary Materials).

An algorithm was implemented to determine the number and duration Δt_{chirp} of the individual frequency ramps, generated for each value of chirp. Given a chirp parameter, the algorithm first computes the frequency bandwidth that would be addressed in the ST case, in the entire dwell time ΔT :

$$\Delta f_{\text{ST}} = \alpha \cdot \Delta T \quad (4)$$

Then, depending on the input chirp value, two scenarios may arise:

1. $\Delta f \leq \Delta f_{\text{eff}}$: For very low chirp values, the ramping frequency stays within the high-efficiency window and, therefore, $N_{\text{trigger}} = 1$ and $\Delta t_{\text{chirp}} \sim \Delta T$; this case corresponds to the maximum delivered power level (that we adopt as reference).
2. $\Delta f > \Delta f_{\text{eff}}$: For increasing chirp values, frequency sweeps start exceeding the available Δf_{eff} ; thus in ST mode, we would lose transmission efficiency; the algorithm then iteratively looks for the highest submultiple of the frequency bandwidth, $\Delta f_{\text{MT}} = \Delta f/n$, fulfilling condition 1). When this is reached, the following relation holds:

$$\Delta t_{\text{chirp}} = \frac{\Delta f}{\alpha \cdot n} = \frac{\Delta T}{n} \quad (5)$$

Then, considering the access time constraint, a binary decision must be taken:

3. $\Delta t_{\text{chirp}} > dt$: In this case, the number of applied ramp triggers is simply provided by

$$N_{\text{trigger}} = \frac{\Delta T}{\Delta T/n} = n \quad (6)$$

4. $\Delta t_{\text{chirp}} < dt$: For high chirp values ($\alpha > 0.25$ MHz/ μ s). In this scenario, where ghost images would appear, the algorithm forces $\Delta t_{\text{chirp}} = dt = 4 \mu$ s and $N_{\text{trigger}} = \Delta T/\Delta t_{\text{chirp}}$ recomputing the ramping bandwidth as $\Delta f = |\alpha| \cdot dt_{\text{chirp}}$ accordingly. This configuration, exceeding the available high-efficiency Δf_{eff} , is inherently related to a worse transmission efficiency with respect to the maximum reference level

Table 1 reports the frequency sweep bandwidth, the number of triggers and the chirping time computed for different chirp values. The transmission efficiency of the second stage as a function of the frequency addressed is shown in Figure 2A,B (for further details, see Figure S2D in Supplementary Materials). The bandwidths related to the ST and MT cases are displayed in blue and orange, respectively. The two panels show two different scenarios, that is, a low chirp case ($\alpha = 0.2$ MHz/ μ s; Figure 2A) and a high chirp case ($\alpha = 0.5$ MHz/ μ s; Figure 2B). The number of triggers is indicated for the MT modality. As it can be observed, the repetition of a signal inside the high-transmission window is favorable with respect to a single scan in the whole dwell time because more energy is globally released on the sample.

The driving RF signals used in the ST and MT scanning modes are schematized in Figure 2C, along with the simulated integrated signal on the PMT. This clearly depicts the increase in delivered power to the target volume in MT mode as a function of time. It is worth recalling that the beam lateral deflection depends on the difference between the central frequencies of the chirps sent simultaneously to the coupled AODs (ie, the ones corresponding to the same axis in each stage; Equation 1).

Even though the acoustic frequencies change in time, in each moment, the frequency difference remains constant. Thus, the beam position is stable during the dwell time.

To demonstrate the improved photostimulation performance of the devised method, we light-targeted a homogeneous fluorescent sample (Autofluorescent Plastic Slides 92 001, Chroma Technology Corp.) and detected the resulting fluorescent signal with the PMT. The measure was repeated varying the chirp parameter symmetrically around 0 MHz/ μ s, alternating ST and MT configurations. For each considered chirp value, we illuminated a ROI located in the center of the optical FOV by means of a 10×10 points 2D raster scanning, that is, $n = 100$ planar coordinates, adopting a dwell time of 20 μ s. For both the trigger modalities, the PMT integration time was set at 20 μ s, equal to the scanning dwell time. The results reported in Figure 2D reveal the different intensity trends obtained for the ST and MT modes, as a function of the chirp α . The signal collected in the unchirped configuration, $\alpha = 0$ MHz/ μ s, exhibits no differences between the two triggering techniques since in both modes the AOD-driving RF can be maintained within the high-efficiency bandwidth for the entire point-to-point switching period. On the other hand, the relative enhancement of the collected fluorescence intensity due to the MT mode grows with increasing absolute chirp values, in accordance with the progressive increase in the effective light-targeting time, with respect to the ST approach. Furthermore, the results demonstrate enhanced power distribution homogeneity, showing values larger than 70% of the maximum power delivered to the inherent focal plane of the objective when performing an axial scan in MT mode, varying the chirp between +1 MHz/ μ s and -1 MHz/ μ s. Interestingly, in Figure 2D, we nevertheless observe an asymmetry, probably related to light scattering in the material, with higher intensity levels attained in more superficial planes, with respect to the inherent objective focal plane, targeted by means of negative chirps.

Chirp (MHz/ μ s)	0	0.05	0.1	0.15	0.2	0.25	>0.25	0.5	1	2
Δf_{ST} (MHz)	0	1	2	3	4	5	>5	10	20	40
Δf_{MT} (MHz)	0	1	1	1	1	1	>1	2	4	8
N_{trigger}	1	1	2	3	4	5	5	5	5	5
Δt_{chirp} (μ s)	20	20	10	6.66	5	4	4	4	4	4

Note: The table color code follows the cases described in the algorithm in paragraph 3.1: Blue cells refer to the ST mode, red cells refer to the best configuration in terms of energy released, orange cells refer to low chirp cases and yellow cells refer to high chirp cases ($\alpha > 0.25$ MHz/ μ s). Chirping times shown in red are constrained by the minimum AOD access time, $dt = 4 \mu$ s.

Abbreviation: AOD, Acousto-optic deflector.

TABLE 1 Number of triggers, effective bandwidth addressed and corresponding chirping times estimated for different chirp values

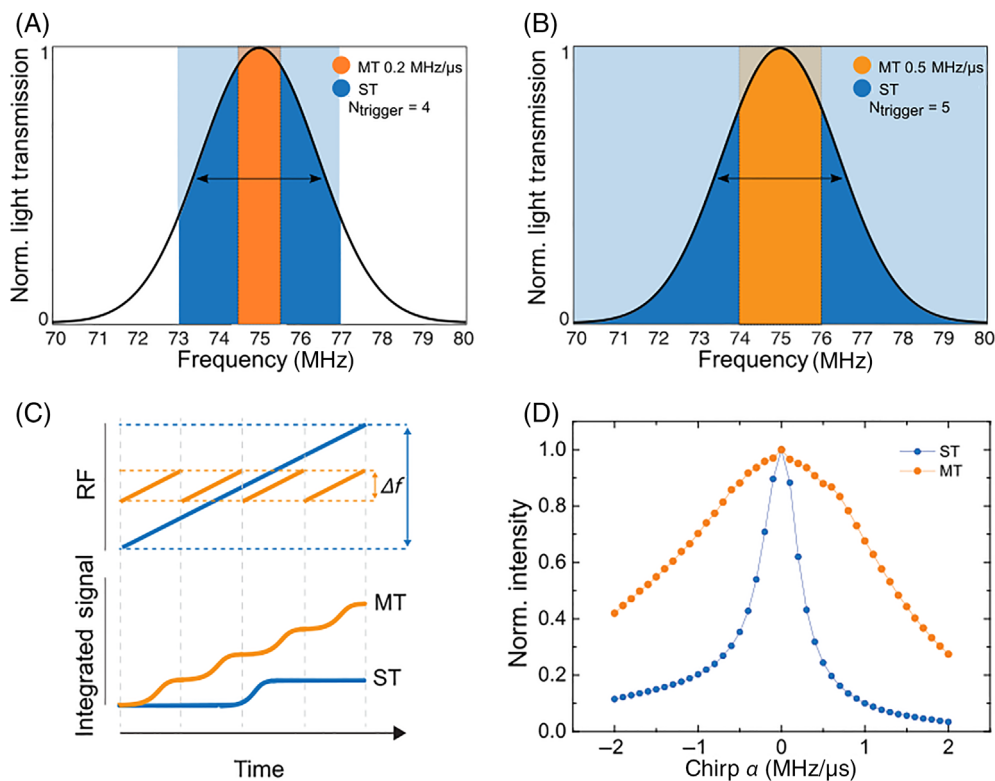


FIGURE 2 A,B. Transmission efficiency of the second stage as a function of the acoustic frequency driving the AOD. The bandwidths addressed in the ST and MT modes are colored in blue and orange, respectively. A, Low chirp case: $\alpha = 0.2$ MHz/ μ s. B, High chirp case: $\alpha = 0.5$ MHz/ μ s. The number of triggers is indicated for the MT modality. C, Top: Schematic of the RF signals used to drive each AOD in the ST (blue) and MT (orange) modes. After the chirp α is defined, a frequency ramp is generated once (single trigger) or repeated multiple times (multitrigger) within the dwell time window. Bottom: The simulated integrated signal collected by the PMT. D, Normalized fluorescence signal collected by the PMT as a function of the applied chirp, addressing light in separate planes with ST (blue) and MT (orange) configurations; 2D raster scans are obtained by illuminating 10×10 points with a dwell time of 20μ s. The integration time of the PMT was set consistently to 20μ s. AOD, Acousto-optic deflector; MT, multitrigger; ST, single trigger

3.2 | 2P optogenetic stimulation with AODs in zebrafish larvae

To demonstrate the performance and improvements of our novel method for AOD-based in vivo photostimulation over the addressable volume, we performed optogenetic stimulation experiments in zebrafish larvae expressing the red-shifted channelrhodopsin variant ReaChR. We used electrophysiological recordings (LFP) as a readout of neuronal activity from displaced planes involving clusters of cells. Figure 3A schematically shows the experimental setup adopted to optically stimulate and electrically record neuronal activity in zebrafish larvae. We successfully evoked LFP responses by light-targeting ROIs of $20 \times 20 \mu\text{m}^2$ at 50-70 mW (peak laser power recorded at the inherent objective focal position). During AOD axial scanning, the chirping frequencies driving the devices varied, with α modulated between -2 MHz/ μ s and $+2$ MHz/ μ s (with 1 MHz/ μ s steps; Figure 3B): This enabled to light-target axially displaced planes of ROIs selected in the hindbrain area.

To exclude any nonoptogenetic effect of the laser stimulation (ie, photoinduced currents or thermal effects), a specific zebrafish larva lacking the optogenetic actuator but expressing the genetically encoded calcium indicator GCaMP6s was used. By exploiting the fluorescent indicator signal, we oriented the light targeting and we addressed the reference ROI for stimulation. Figure 3C reports two average activity traces recorded in the larva expressing GCaMP and ReaChR, relatively time-shifted to match the triggers. No evident potential changes were elicited in the GCaMP larva under light stimulation, while the ReaChR larva showed a clear evoked LFP response, under the same stimulation parameters. In particular, the full stimulation time was $\Delta T_{\text{tot}} = 12.5$ ms for both cases. This comparison proved the specificity of the stimulation system ruling out any artifacts due to photoinduced currents on the microelectrode or any thermal effects correlated with infrared illumination warming of the sample.

Fluorescence of the reporter TagRFP was used to confirm the ReaChR expression: Figure 3D shows the

fluorescence image of the larval zebrafish hindbrain acquired using the GM scanning head. The fluorescent electrode tip is visible inside the orange square, which indicates the ROI selected for AOD light targeting. Since neurons are tightly packed in zebrafish larvae, given the size of the stimulation ROI of $400 \mu\text{m}^2$ and the typical size of neuron bodies in this organism (5-7 μm), it can be estimated that the clusters stimulated within each ROI were composed of 8 to 16 cells. These were illuminated with beam spots having a lateral size corresponding to

the measured PSF of $d = 1.2 \mu\text{m}$ (for further detail, see Figure S2F in Supplementary Materials).

To compare the conventional ST mode with our MT strategy, two different stimulation experiments were carried on zebrafish larvae expressing ReaChR in all neurons. First, the effect was evaluated by continuously stimulating a stack of overlaid planes through AOD axial scanning. The LFP amplitudes recorded in response to the two stimulation strategies were compared (Figure 3E). It was observed that the MT configuration

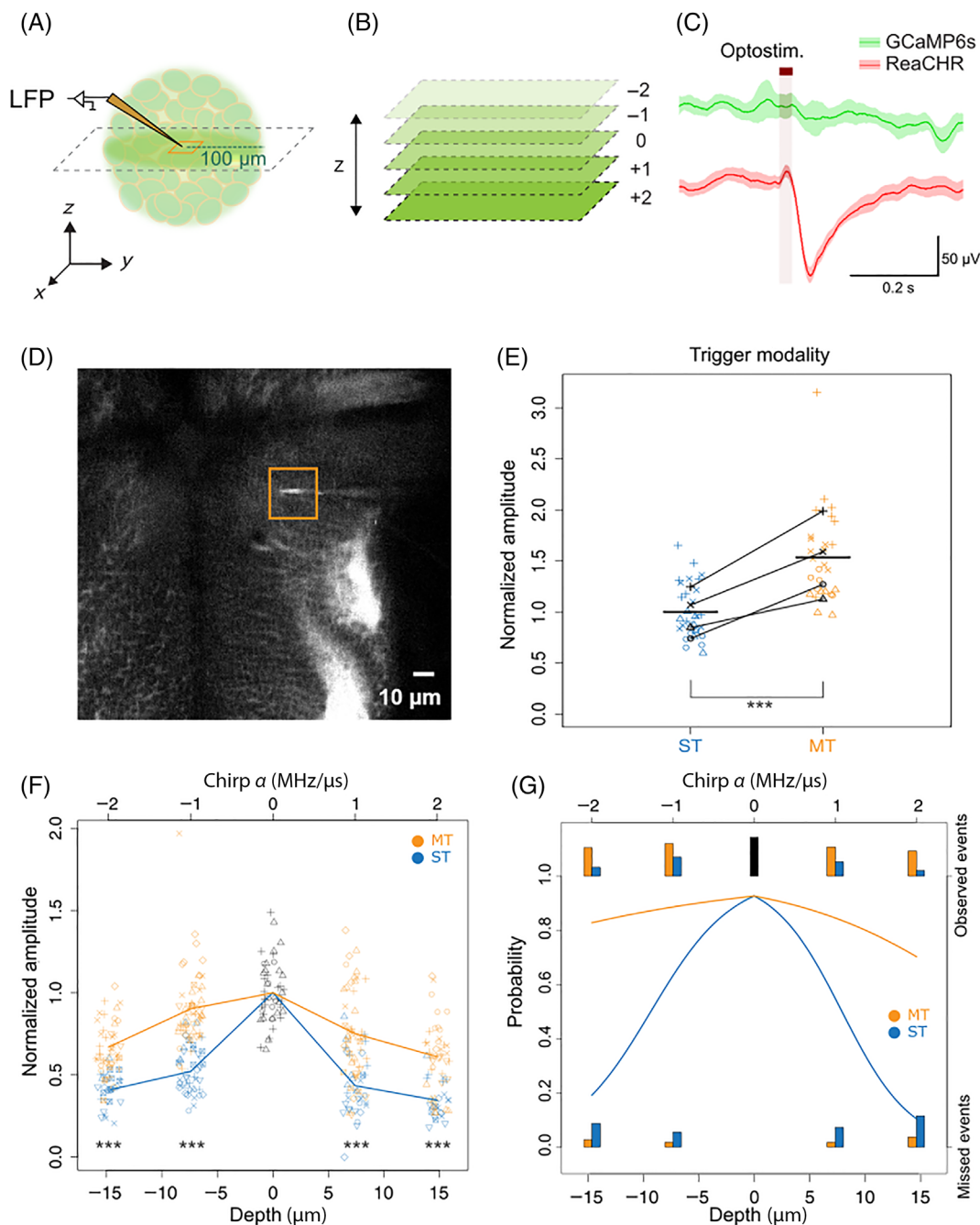


FIGURE 3 Legend on next page.

was associated with a significantly larger amplitude response with respect to ST (+54% between the average values of the two configurations, P value $< .0001$). This indicated a significant increase in the neuronal activity induced by a volume photostimulation exploiting the MT modality. The latter, as expected, provided enhanced optogenetic neuronal stimulation efficiency since it delivered the excitation light for longer periods, within the same dwell time, compared to the ST mode.

Next, the effect of the two triggering modalities was tested on optogenetic stimulations of separate planes individually addressed in the aforementioned range of chirp values (Figure 3F). With respect to the unchirped condition, amplitudes of events evoked with positive or negative chirp values were smaller. Nevertheless, amplitudes evoked in the MT configuration were larger than those recorded with the ST configuration for every chirp value, confirming the conclusions of the first experiment (P value $< .0001$ for each comparison between ST and MT). The normalized average peak amplitude differences between events evoked in the MT and ST configurations are reported in the Supplementary Materials in Table S1 for every chirp value.

Finally, the probabilities to observe an optogenetically induced neuronal activation in the two triggering configurations were compared as a function of the different chirp values (Figure 3G). The number of recorded events is reported in Table S2 in the Supplementary Materials. As in the former experiment, it was observed that positive or negative chirp parameters decreased the probability to observe an event with respect to the unchirped case (0 MHz/ μ s). However, the MT strategy significantly compensated for

this phenomenon with respect to the ST mode, greatly reducing the gap with the unchirped condition.

Notably, the probability curve was asymmetric, decreasing more rapidly for positive chirp values. This behavior reflected the analogous trend found testing the fluorescent signal detected in a homogeneous fluorescent sample, where larger energy delivery was shown to be related to negative chirps with respect to the positive ones: This is due to the shorter light propagation and the reduced scattering effects in the sample.

Interestingly, in the MT modality, an activation probability always larger than 75% was observed for all the chirp values, in opposition to the low efficacy in using ST light stimulation with nonzero chirp values. This demonstrated that there is an almost uniform probability distribution to optogenetically trigger the neuronal activation in all the addressable volume when adopting the MT photostimulation method.

Overall, these results exhibited how the proposed method allowed unprecedented 3D 2P optostimulation in zebrafish larvae by means of AODs. Pushing up the energy distribution deliverable in the volume, we observed a remarkably uniform neuronal response and activation probability, validating the use of AODs for effective 3D photostimulation.

4 | DISCUSSION

2P optogenetic stimulation requires proper tools to efficiently access 3D broadly distributed neuronal populations and sufficient speed to address them quasi-

FIGURE 3 A, Schematic of the electrophysiological recording setup. The pipette tip was positioned in the center of the ROI (orange square) addressed by light stimulation. The dashed gray square indicates the plane selected by the AOD scanning stage. 2D raster scans of 20×20 pts were repeated to reach the maximum evocable peak amplitudes, obtained after $n = 5$ stimulation cycles with a dwell time $\Delta T = 20 \mu$ s. B, Schematic of AOD axial scanning where the chirp parameter is modulated from -2 MHz/ μ s to $+2$ MHz/ μ s, addressing different planes. Each chirp unitary step corresponds to an axial shift of 7.70μ m with respect to the inherent objective focal position. C, Representative average LFP traces were recorded in zebrafish larvae expressing GCaMP (green) and with ReaChR (red) in neurons, relatively time-shifted to match the stimulation trigger (brown). The test was repeated for $N = 3$ larvae. The full stimulation time for both the cases was $\Delta T_{\text{tot}} = 12.5$ ms. D, Fluorescence image of larval zebrafish hindbrain acquired using galvo scanning mode. The orange square highlights the ROI selected for AOD light targeting. The fluorescent recording electrode tip is visible inside the ROI. E, Normalized amplitudes of the electrophysiological responses induced in single trigger (ST, blue) or multitrigger (MT, orange) conditions ($n = 1$ scanning cycle for each plane). Data from $N = 4$ zebrafish larvae are indicated by different symbols. Black lines join the average values for each animal. Thick horizontal black lines indicate the global average values in the two conditions. F, Normalized LFP amplitudes evoked in the two trigger conditions as a function of the chirp value. Different symbols indicate data from $N = 7$ zebrafish larvae. Line segments join mean values for each trigger condition and chirp value ($n = 5$ scanning cycles each plane). G, The colored curves indicate the estimated probability to observe an electrophysiological response evoked by light stimulation for the two trigger modalities as a function of the chirp values ($n = 5$ scanning cycles for each plane). Positive and negative events recorded from all the $N = 7$ zebrafish larvae with the two trigger modalities are reported by colored spots, respectively, in the top and bottom areas of the plot, for the corresponding chirp values. E,F, Statistically significant differences between all the comparisons between ST and MT acquisition are indicated by three asterisks (P value $< .0001$). The number of positive and missed events is reported in Supplementary Material in Table S2. AOD, Acousto-optic deflector; LFP, local field potential; Optostim., optostimulation; ROI, region of interest

simultaneously. For example, GM-based scanning approaches are not commonly used in optogenetics because they are characterized by long commutation times due to their intrinsic inertia. Furthermore, for 3D light addressing, GMs require to be coupled with additional devices like electrically tunable lenses [61]. Alternative solutions are the ones provided by holographic illumination through SLM, widely implemented to draw random-access trajectories and simultaneously stimulate multiple regions. Still, the refresh time required to modulate the stimulation pattern remains substantial; moreover, this approach is hindered by laser power splitting among different targets. AODs have been recently utilized in light-targeting applications for their fast dynamics and high refresh rate, being suited for near-simultaneous multisite access in distant brain districts. However, demonstrating the near-simultaneous illumination of multiple targets with AODs was out of the scope of this work. On the other hand, we addressed the reason why AODs have not been used in volume photostimulation applications yet, especially those exploiting 2P excitation. This is due to the non-uniform light-power delivery when stimulating axially dislocated regions with equal light-addressing time. In order to compensate for this drawback, dedicated software modules are often employed to adjust the amplitude of the RFs driving the AODs for each addressable coordinate so as to produce a lowered flat power distribution across the scanned volume.

Here, we present a novel solution to face this challenge, able to raise the axial power delivery toward the maximum value obtainable on the objective reference focal plane. In order to improve the released power, we repeatedly triggered the chirps driving the AODs before activating a new frequency configuration in the DDS for the repositioning of the laser beam, effectively multiplying the minimum energy deposited as a function of the addressed plane.

This improvement enables 2P applications with AODs that were precluded until now. In this regard, we proved the 2P photoactivation of optogenetic actuators in 3D in zebrafish larvae, demonstrating the advantages provided by the proposed multitrigged stimulation strategy. In particular, we showed how the probability to optogenetically elicit an electrophysiological response in separated planes and its relative amplitude is increased thanks to the prolonged light delivery time. 2P photostimulation of cellular clusters in dislocated planes represents an unprecedented result with AODs, obtained here for the first time by surmounting the loss in light transmission during axial scanning.

However, since the scanning FOV and the axial range are directly determined by the specific optics adopted, these dimensions can be therefore improved under certain physical constraints. The method we devised allows

us to extend the axial range where the light is efficiently addressed with AODs, independently of the specific features of the optical setup, without affecting the point spread function of the system.

For what concerns the chromatic dispersion undergone by the diffracted beam—a typical issue to deal with when diffraction gratings are involved—we partially compensated it by placing the second pair of AODs symmetrically opposite to the first one (see Supplementary Materials for details). In such a way, the dispersion effect is counterbalanced owing to an inverted deflection of the broadband laser, which globally increases the symmetry of the beam profile. Further upgrades regarding spatial dispersion and group velocity dispersion would involve specific achromatic optics or compensating systems. Anyway, all the experimental tests were out addressing a uniform lateral FOV, as shown in Supplementary Materials.

The proof of principle of this innovative method resides in the AOD module optimization and in the advanced digital control system driving these devices. Therefore, it is directly applicable to all those setups that already leverage AODs for fast axial scanning, 3D multisite imaging and random-access light targeting. Furthermore, here we designed a fast 2P 3D scanning head for photostimulation as a self-standing system, coupled in this case with a fixed-stage microscope specifically tailored for electrophysiology applications and microscopy in the infrared range. Nonetheless, such a system can represent an add-on module for existing microscopes. Indeed, applying this AOD-based photostimulation head as an add-on to a whole-brain imaging system, such as a light-sheet fluorescence microscope [62, 63], would open the way to numerous further experimental possibilities, toward all optical methods [64, 65]. Fast axial-light addressing, large FOV and deep optical access, also guaranteed by 2P excitation, will help in opening new neuroscience scenarios. Interestingly, these advancements are expected to enhance the functional mapping of complex neuronal circuits and to understand the causality between nervous operational pathway activations and behaviors.

ACKNOWLEDGMENT

Open Access Funding provided by Università degli Studi di Firenze within the CRUI-CARE Agreement.

CONFLICT OF INTEREST

The authors declare no conflicts of interest.

AUTHOR CONTRIBUTIONS

Pietro Ricci: Writing – original draft; writing – review and editing; multitrigged light stimulation modality devising; optical setup characterization and the optical

experimental measurements; electrophysiological and optogenetics in vivo measurements; data collection and processing; results discussion. **Marco Marchetti**: Graphical user interface design; multitriggered light stimulation modality devising; system electronics design; optical setup characterization and the optical experimental measurements; writing – review and editing; results discussion. **Michele Sorelli**: AOD beam-scanning unit software design and development; multitriggered light stimulation modality devising; writing – review and editing; results discussion. **Vladislav Gavryusev**: AOD beam-scanning unit software design and development; system electronics design; optical setup characterization; optical experimental measurements supervision; writing – review and editing; results discussion. **Lapo Turrini**: elavl3:ReaChR-TagRFP zebrafish line generation; electrophysiological and optogenetics in vivo measurements; data collection and processing; writing – review and editing; results discussion. **Francesco Vanzi**: Zebrafish research supervision; writing – review and editing; results discussion. **Francesco Resta**: Electrophysiological and optogenetics in vivo measurements; data collection and processing; writing – review and editing; results discussion. **Giuseppe de Vito**: In vivo data analysis; writing – review and editing; results discussion. **Giuseppe Sancataldo**: Optical design conception and artworks editing assistance; writing – review and editing; results discussion. **Ludovico Silvestri**: Project and experiments supervision; writing – review and editing; results discussion. **Francesco Saverio Pavone**: Experiments design and research initiation; writing – review and editing; results discussion.

DATA AVAILABILITY STATEMENT

Data underlying the results presented in this paper are not publicly available at this time but may be obtained from the authors upon reasonable request.

ETHICS STATEMENT

All experiments involving zebrafish larvae were carried out in accordance with Italian law on animal experimentation (D.L. March 2014, n.26), under authorization n.606/2020-PR from the Italian Ministry of Health.

ORCID

Pietro Ricci  <https://orcid.org/0000-0002-6931-9234>

REFERENCES

- [1] E. Ronzitti, V. Emiliani, E. Papagiakoumou, *Front. Cell. Neurosci.* **2018**, *12*, 469. <https://doi.org/10.3389/fncel.2018.00469>.
- [2] G. J. Broussard, R. Liang, L. Tian, *Front. Mol. Neurosci.* **2014**, *7*, 97. <https://doi.org/10.3389/fnmol.2014.00097>.
- [3] M. Z. Lin, M. J. Schnitzer, *Nat. Neurosci.* **2016**, *19*, 1142. <https://doi.org/10.1038/nn.4359>.
- [4] K. Deisseroth, *Nat. Methods* **2011**, *8*, 26. <https://doi.org/10.1038/nmeth.f.324>.
- [5] O. Yizhar, L. E. Fenno, T. J. Davidson, M. Mogri, K. Deisseroth, *Neuron* **2011**, *71*, 9. <https://doi.org/10.1016/j.neuron.2011.06.004>.
- [6] T. W. Chen, T. J. Wardill, Y. Sun, S. R. Pulver, S. L. Renninger, A. Baohan, E. R. Schreiter, R. A. Kerr, M. B. Orger, V. Jayaraman, L. L. Looger, K. Svoboda, D. S. Kim, *Nature* **2013**, *499*, 295. <https://doi.org/10.1038/nature12354>.
- [7] H. Dana, Y. Sun, B. Mohar, B. K. Hulse, A. M. Kerlin, J. P. Hesseman, G. Tsegaye, A. Tsang, A. Wong, R. Patel, J. J. Macklin, Y. Chen, A. Konnerth, V. Jayaraman, L. L. Looger, E. R. Schreiter, K. Svoboda, D. S. Kim, *Nat. Methods* **2019**, *16*, 649. <https://doi.org/10.1038/s41592-019-0435-6>.
- [8] W. R. Zipfel, R. M. Williams, W. W. Webb, *Nat. Biotechnol.* **2003**, *21*, 1369. <https://doi.org/10.1038/nbt899>.
- [9] K. Svoboda, R. Yasuda, *Neuron* **2006**, *50*, 823. <https://doi.org/10.1016/j.neuron.2006.05.019>.
- [10] F. Helmchen, W. Denk, *Nat. Methods* **2005**, *2*, 932. <https://doi.org/10.1038/nmeth818>.
- [11] W. Denk, J. H. Strickler, W. W. Webb, *Science* **2008**, *248*, 73.
- [12] J. Lakowicz, *Principles of Fluorescence Spectroscopy*, Springer, **2013**. <https://doi.org/10.1007/978-0-387-46312-4>.
- [13] L. Petreanu, T. Mao, S. M. Sternson, K. Svoboda, *Nature* **2009**, *457*, 1142. <https://doi.org/10.1038/nature07709>.
- [14] H. Wang, J. Peca, M. Matsuzaki, K. Matsuzaki, J. Noguchi, L. Qiu, D. Wang, F. Zhang, E. Boyden, K. Deisseroth, H. Kasai, W. C. Hall, G. Feng, G. J. Augustine, *Proc. Natl. Acad. Sci. U. S. A.* **2007**, *104*, 8143. <https://doi.org/10.1073/pnas.0700384104>.
- [15] J. P. Rickgauer, D. W. Tank, *Proc. Natl. Acad. Sci.* **2009**, *106*, 15025. <https://doi.org/10.1073/PNAS.0907084106>.
- [16] S. Gasparini, J. C. Magee, *J. Neurosci.* **2006**, *26*, 2088. <https://doi.org/10.1523/JNEUROSCI.4428-05.2006>.
- [17] E. Ronzitti, C. Ventalon, M. Canepari, B. C. Forget, E. Papagiakoumou, V. Emiliani, *J. Opt. (United Kingdom)* **2017**, *19*, 113001. <https://doi.org/10.1088/2040-8986/aa8299>.
- [18] E. J. Botcherby, M. J. Booth, R. Juskaitis, T. Wilson, *Opt. Lett.* **2007**, *32*, 2007. <https://doi.org/10.1364/OL.32.002007>.
- [19] E. J. Botcherby, R. Juškaitis, M. J. Booth, T. Wilson, *Opt. Commun.* **2008**, *281*, 880. <https://doi.org/10.1016/J.OPTCOM.2007.10.007>.
- [20] W. Göbel, F. Helmchen, *Phys. Ther.* **2007**, *22*, 358. <https://doi.org/10.1152/physiol.00032.2007>.
- [21] C. G. Durfee, E. E. Hoover, J. A. Squier, R. Carriles, T. A. Planchon, W. Amir, *Opt. Lett.* **2007**, *32*, 1731. <https://doi.org/10.1364/OL.32.001731>.
- [22] A. M. Packer, D. S. Peterka, J. J. Hirtz, R. Prakash, K. Deisseroth, R. Yuste, *Nat. Methods* **2012**, *9*, 1202. <https://doi.org/10.1038/nmeth.2249>.
- [23] I. W. Chen, E. Ronzitti, B. R. Lee, T. L. Daigle, H. Zeng, E. Papagiakoumou, V. Emiliani, Parallel holographic illumination enables sub-millisecond two-photon optogenetic activation in mouse visual cortex in vivo, *bioRxiv*, **2018**, *1*, doi: <https://doi.org/10.1101/250795>.
- [24] N. Grossman, V. Poher, M. S. Grubb, G. T. Kennedy, K. Nikolic, B. McGovern, R. B. Palmimi, Z. Gong, E. M. Drakakis,

- M. AANeil, M. D. Dawson, J. Burrone, P. Degenaar, *J. Neural Eng.* **2010**, *7*, 16004. <https://doi.org/10.1088/1741-2560/7/1/016004>.
- [25] N. Farah, I. Reutsky, S. Shoham, *Annu. Int. Conf. IEEE Eng. Med. Biol. - Proc.* **2007**, *2007*, 6368. <https://doi.org/10.1109/IEMBS.2007.4353812>.
- [26] S. Wang, S. Szobota, Y. Wang, M. Volgraf, Z. Liu, C. Sun, D. Trauner, E. Y. Isacoff, X. Zhang, *Nano Lett.* **2007**, *7*, 3859. <https://doi.org/10.1021/nl072783t>.
- [27] P. Zhu, O. Fajardo, J. Shum, Y. P. Zhang Schärer, R. W. Friedrich, *Nat. Protoc.* **2012**, *7*, 1410. <https://doi.org/10.1038/nprot.2012.072>.
- [28] Y. Xue, L. Waller, H. Adesnik, and N. Pégard, Three-dimensional multi-site random access photostimulation (3D-MAP), *bioRxiv*, **2020**, *1*, doi: <https://doi.org/10.1101/2020.06.28.176503>.
- [29] J. N. Stirman, M. M. Crane, S. J. Husson, S. Wabnig, C. Schultheis, A. Gottschalk, H. Lu, *Nat. Methods* **2011**, *8*, 153. <https://doi.org/10.1038/nmeth.1555>.
- [30] E. Papagiakoumou, F. Anselmi, A. Bègue, V. de Sars, J. Glückstad, E. Y. Isacoff, V. Emiliani, *Nat. Methods* **2010**, *7*, 848. <https://doi.org/10.1038/nmeth.1505>.
- [31] E. Chaigneau, E. Ronzitti, M. A. Gajowa, G. J. Soler-Llavina, D. Tanese, A. Y. Brureau, E. Papagiakoumou, H. Zeng, V. Emiliani, *Front. Cell. Neurosci.* **2016**, *10*, 234. <https://doi.org/10.3389/fncel.2016.00234>.
- [32] V. Emiliani, A. E. Cohen, K. Deisseroth, M. Häusser, *J. Neurosci.* **2015**, *35*, 13917. <https://doi.org/10.1523/JNEUROSCI.2916-15.2015>.
- [33] A. Picot, S. Dominguez, C. Liu, I. W. Chen, D. Tanese, E. Ronzitti, P. Berto, E. Papagiakoumou, D. Oron, G. Tessier, B. C. Forget, V. Emiliani, *Cell Rep.* **2018**, *24*, 1243. <https://doi.org/10.1016/j.celrep.2018.06.119>.
- [34] J. Y. Lin, *Exp. Physiol.* **2011**, *96*, 19. <https://doi.org/10.1113/expphysiol.2009.051961>.
- [35] M. Duocastella, S. Surdo, A. Zunino, A. Diaspro, P. Saggau, *J. Phys. Photonics* **2021**, *3*, 12004. <https://doi.org/10.1088/2515-7647/abc23c>.
- [36] M. Duocastella, G. Sancataldo, P. Saggau, P. Ramoino, P. Bianchini, A. Diaspro, *ACS Photonics* **2017**, *4*, 1797. <https://doi.org/10.1021/acsp Photonics.7b00382>.
- [37] P. Ricci, G. Sancataldo, V. Gavryusev, A. Franceschini, M. C. Müllenbroich, L. Silvestri, F. S. Pavone, *Biomed. Opt. Express* **2020**, *11*, 3111. <https://doi.org/10.1364/boe.390916>.
- [38] V. Gavryusev, G. Sancataldo, P. Ricci, A. Montalbano, C. Fornetto, L. Turrini, A. Laurino, L. Pesce, G. de Vito, N. Tiso, F. Vanzi, L. Silvestri, F. S. Pavone, *J. Biomed. Opt.* **2019**, *24*(10), 1. <https://doi.org/10.1117/1.jbo.24.10.106504>.
- [39] G. Sancataldo, V. Gavryusev, G. de Vito, L. Turrini, M. Locatelli, C. Fornetto, N. Tiso, F. Vanzi, L. Silvestri, F. S. Pavone, *Front. Neuroanat.* **2019**, *13*, 7. <https://doi.org/10.3389/fnana.2019.00007>.
- [40] R. J. Cotton, E. Froudarakis, P. Storer, P. Saggau, A. S. Tolias, *Front. Neural Circuits* **2013**, *7*, 151. <https://doi.org/10.3389/fncir.2013.00151>.
- [41] T. Fernández-Alfonso, K. M. N. S. Nadella, M. F. Iacaruso, B. Pichler, H. Roš, P. A. Kirkby, R. A. Silver, *J. Neurosci. Methods* **2014**, *222*, 69. <https://doi.org/10.1016/j.jneumeth.2013.10.021>.
- [42] G. Szalay, L. Judák, G. Katona, K. Ócsai, G. Juhász, M. Veress, Z. Szadai, A. Fehér, T. Tompa, B. Chiovini, P. Maák, B. Rózsa, *Neuron* **2016**, *92*, 723. <https://doi.org/10.1016/j.neuron.2016.10.002>.
- [43] G. D. Reddy, P. Saggau, *Cold Spring Harb. Protoc.* **2013**, *8*(1), 1. <https://doi.org/10.1101/pdb.top072603>.
- [44] G. Duemani Reddy, K. Kelleher, R. Fink, P. Saggau, *Nat. Neurosci.* **2008**, *11*, 713. <https://doi.org/10.1038/nn.2116>.
- [45] V. Iyer, T. M. Hoogland, P. Saggau, *J. Neurophysiol.* **2006**, *95*, 535. <https://doi.org/10.1152/jn.00865.2005>.
- [46] B. F. Grewe, D. Langer, H. Kasper, B. M. Kampa, F. Helmchen, *Nat. Methods* **2010**, *7*, 399. <https://doi.org/10.1038/nmeth.1453>.
- [47] R. Salomé, Y. Kremer, S. Dieudonné, J. F. Léger, O. Krichevsky, C. Wyart, D. Chatenay, L. Bourdieu, *J. Neurosci. Methods* **2006**, *154*, 161. <https://doi.org/10.1016/j.jneumeth.2005.12.010>.
- [48] Y. Otsu, V. Bormuth, J. Wong, B. Mathieu, G. P. Dugué, A. Feltz, S. Dieudonné, *J. Neurosci. Methods* **2008**, *173*, 259. <https://doi.org/10.1016/j.jneumeth.2008.06.015>.
- [49] G. Katona, G. Szalay, P. Maák, A. Kaszás, M. Veress, D. Hillier, B. Chiovini, E. S. Vizi, B. Roska, B. Rózsa, *Nat. Methods* **2012**, *9*, 201. <https://doi.org/10.1038/nmeth.1851>.
- [50] M. Marosi, G. Szalay, G. Katona, B. Rózsa, *Neuromethods* **2019**, *148*, 335. https://doi.org/10.1007/978-1-4939-9702-2_14.
- [51] G. Szalay, L. Judák, Z. Szadai, B. Chiovini, D. Mezey, D. Pálfi, M. Madarász, K. Ócsai, F. Csikor, M. Veress, P. Maák, G. Katona, *Orv. Hetil.* **2015**, *156*, 2120. <https://doi.org/10.1556/650.2015.30329>.
- [52] Y. Liu, Y. Zhao, X. Lv, Y. Li, X. Zhang, J. Zhang, L. Wang, S. Zeng, *Rev. Sci. Instrum.* **2012**, *83*, 025116.
- [53] K. Wang, Y. Liu, Y. Li, Y. Guo, P. Song, X. Zhang, S. Zeng, Z. Wang, *PLoS One* **2011**, *6*, e28468. <https://doi.org/10.1371/journal.pone.0028468>.
- [54] G. D. Reddy, P. Saggau, *J. Biomed. Opt.* **2005**, *10*, 064038. <https://doi.org/10.1117/1.2141504>.
- [55] J. Y. Lin, P. M. Knutsen, A. Muller, D. Kleinfeld, R. Y. Tsien, *Nat. Neurosci.* **2013**, *16*, 1499. <https://doi.org/10.1038/nn.3502>.
- [56] T. W. Dunn, C. Gebhardt, E. A. Naumann, C. Riegler, M. B. Ahrens, F. Engert, F. del Bene, *Neuron* **2016**, *89*, 613. <https://doi.org/10.1016/j.neuron.2015.12.021>.
- [57] N. Vladimirov, Y. Mu, T. Kawashima, D. V. Bennett, C. T. Yang, L. L. Looger, P. J. Keller, J. Freeman, M. B. Ahrens, *Nat. Methods* **2014**, *11*, 883. <https://doi.org/10.1038/nmeth.3040>.
- [58] M. C. Müllenbroich, L. Turrini, L. Silvestri, T. Alterini, A. Gheisari, N. Tiso, F. Vanzi, L. Sacconi, F. S. Pavone, *Front. Cell. Neurosci.* **2018**, *12*, 315. <https://doi.org/10.3389/fncel.2018.00315>.
- [59] M. Westerfield, *The Zebrafish Book: A Guide for the Laboratory Use of Zebrafish*, University of Oregon Press, Eugene **2000**. http://zfin.org/zf_info/zfbook/zfbk.html (accessed: April 2021).
- [60] L. Turrini, C. Fornetto, G. Marchetto, M. C. Müllenbroich, N. Tiso, A. Vettori, F. Resta, A. Masi, G. Mannaioni, F. S. Pavone, F. Vanzi, *Sci. Rep.* **2017**, *7*(1), 1. <https://doi.org/10.1038/s41598-017-03087-z>.
- [61] N. Vladimirov, C. Wang, B. Höckendorf, A. Pujala, M. Tanimoto, Y. Mu, C. T. Yang, J. D. Wittenbach, J. Freeman, S.

- Preibisch, M. Koyama, P. J. Keller, M. B. Ahrens, *Nat. Methods* **2018**, *15*, 1117. <https://doi.org/10.1038/s41592-018-0221-x>.
- [62] M. B. Ahrens, M. B. Orger, D. N. Robson, J. M. Li, P. J. Keller, *Nat. Methods* **2013**, *10*, 413. <https://doi.org/10.1038/nmeth.2434>.
- [63] G. de Vito, L. Turrini, M. C. Muellenbroich, P. Ricci, G. Sancataldo, G. Mazzamuto, N. Tiso, L. Sacconi, D. Fanelli, L. Silvestri, F. Vanzi, F. Pavone, *Biomed. Opt. Express* **2021**. <https://doi.org/10.1364/BOE.434146>.
- [64] L. Fan, *Doctoral dissertation*, Graduate School of Arts & Sciences, Harvard University **2019**.
- [65] Y. Adam, *J. Neurosci. Methods* **2021**, *353*, 109101. <https://doi.org/10.1016/J.JNEUMETH.2021.109101>.

SUPPORTING INFORMATION

Additional supporting information may be found in the online version of the article at the publisher's website.

How to cite this article: P. Ricci, M. Marchetti, M. Sorelli, L. Turrini, F. Resta, V. Gavryusev, G. de Vito, G. Sancataldo, F. Vanzi, L. Silvestri, F. S. Pavone, *J. Biophotonics* **2022**, *15*(4), e202100256. <https://doi.org/10.1002/jbio.202100256>